# Delocalized Electron Engineering of MXene-Immobilized Atomic Catalysts toward Fast Desolvation and Dendritic Inhibition for Low-Temperature Zn Metal Batteries

Jing Zhang,* Lu Pan, Lujie Jia, Jing Dong, Caiyin You,* Chenxiao Han, Na Tian, Xiaomin Cheng, Bingbing Tang, Qinghua Guan, Yongzheng Zhang, Bo Deng, Li Lei, Meinan Liu, Hongzhen Lin,* and Jian Wang*

**ABSTRACT:** Rechargeable low-temperature aqueous zinc metal batteries (LT-AZMBs) are considered as a competitive candidate for next-generation energy storage systems owing to increased safety and low cost. Unfortunately, sluggish desolvation kinetics of hydrated $[Zn(H_2O)_x]^{2+}$ and inhomogeneous ion flux cause detrimental hydrogen evolution reactions (HER) and Zn dendrite growth. Herein, the atomic iron well-implanted onto MXene via defect capture (SAFe@MXene) has been initially proposed to modulate Zn plating. The SAFe@MXene serves as kinetic promoters to enhance interfacial desolvation of $[Zn(H_2O)_x]^{2+}$ to prevent HER and uniformizes $Zn^{2+}$ flux for smooth deposition, as confirmed by theoretical simulation, Raman and electrochemical tests. Consequently, under 0 °C, the SAFe@MXene-modulated Zn electrodes deliver long-term stability of 800 h with lower overpotentials even at 5 mA $cm^{-2}$ or higher plating/stripping capacity. The full cell with a $MnO_2$ cathode stabilizes a high capacity-retention of nearly 100% after 1000 cycles at 1 A $g^{-1}$, suggesting great promise for high-performance LT-AZMBs.

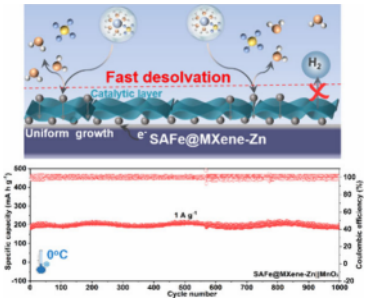


**KEYWORDS:** *Zn metal battery, Low-temperature environment, Catalytic desolvation, Electronic redistribution, Single-atom catalyst*

Rechargeable aqueous zinc metal batteries (AZMBs) are considered to be a promising alternative for future energy storage systems due to the merits of high capacity, low cost, and excellent safety.[1−6] Compared with other anodes, the metallic Zn displays an ultrahigh theoretical capacity (820 mA h $g^{-1}$/5855 mA h $cm^{-3}$) and suitable redox potential (−0.76 V vs standard hydrogen electrode).[7−10] However, the nonuniform $Zn^{2+}$ flux at the electrode/electrolyte interface would exacerbate random diffusion and $Zn^0$ plating, inducing dendrite formation, "dead Zn", and internal short-circuit.[11−14] Meanwhile, the partially dissociated $[Zn(H_2O)_x]^{2+}$ solvation shell incurs the generation of active water in the low-temperature surrounding, resulting in severe hydrogen evolution reactions (HER) and corrosion when getting electrons from the metallic Zn surface.[15−17] Consequently, the Zn anode usually encounters shortened cycling life and very poor Coulombic efficiency (CE), severely hindering practical application of low-temperature AZMBs (LT-AZMBs).[18−20]

Recently, efforts have been devoted to modulations of Zn behaviors by tuning electrolyte components, constructing functional electrodes or current collectors, and fabricating interfacial protective layers.[1,3,21−28] These strategies aim to either inhibit HER through separating active water molecules from a conductive Zn electrode or decrease deposition current density to eliminate large aggregation of dendrite formation.[5,29−34] Similar to a Li metal anode, the Zn plating processes also involve several mass/charge transport steps of $Zn^{2+}$-related species, including the desolvation of $[Zn(H_2O)_x]^{2+}$ clusters to release free $Zn^{2+}$, bare $Zn^{2+}$ transfer across an electrolyte/electrode interface, diffusion/migration of $Zn^{2+}$ or $Zn^0$ along the electrode surface, and $Zn^0$ nucleation and deposition.[35,36] Before plating, the initial dissociation of $[Zn(H_2O)_x]^{2+}$ clusters for generating free $Zn^{2+}$ at the interface is highly decisive to the subsequent electrochemical steps including diffusion, nucleation, and deposition of Zn species.[22,37−39] Integrating an interfacial modulation layer to sieve and dissociate $H_2O$ species is beneficial to uniformize $Zn^{2+}$ flux, thus suppressing the undesirable water-induced HER.[38,40−43] Despite porous metal−organic frameworks (MOFs) enabled by physical pore sieving,[44,45] the electrocatalytic method has been proposed to decrease the related barriers in other battery systems such as Li and Mg batteries.[46−52] Ideally, owing to the higher barriers existing in dissociating $[Zn(H_2O)_x]^{2+}$ clusters, the catalytic sites may also

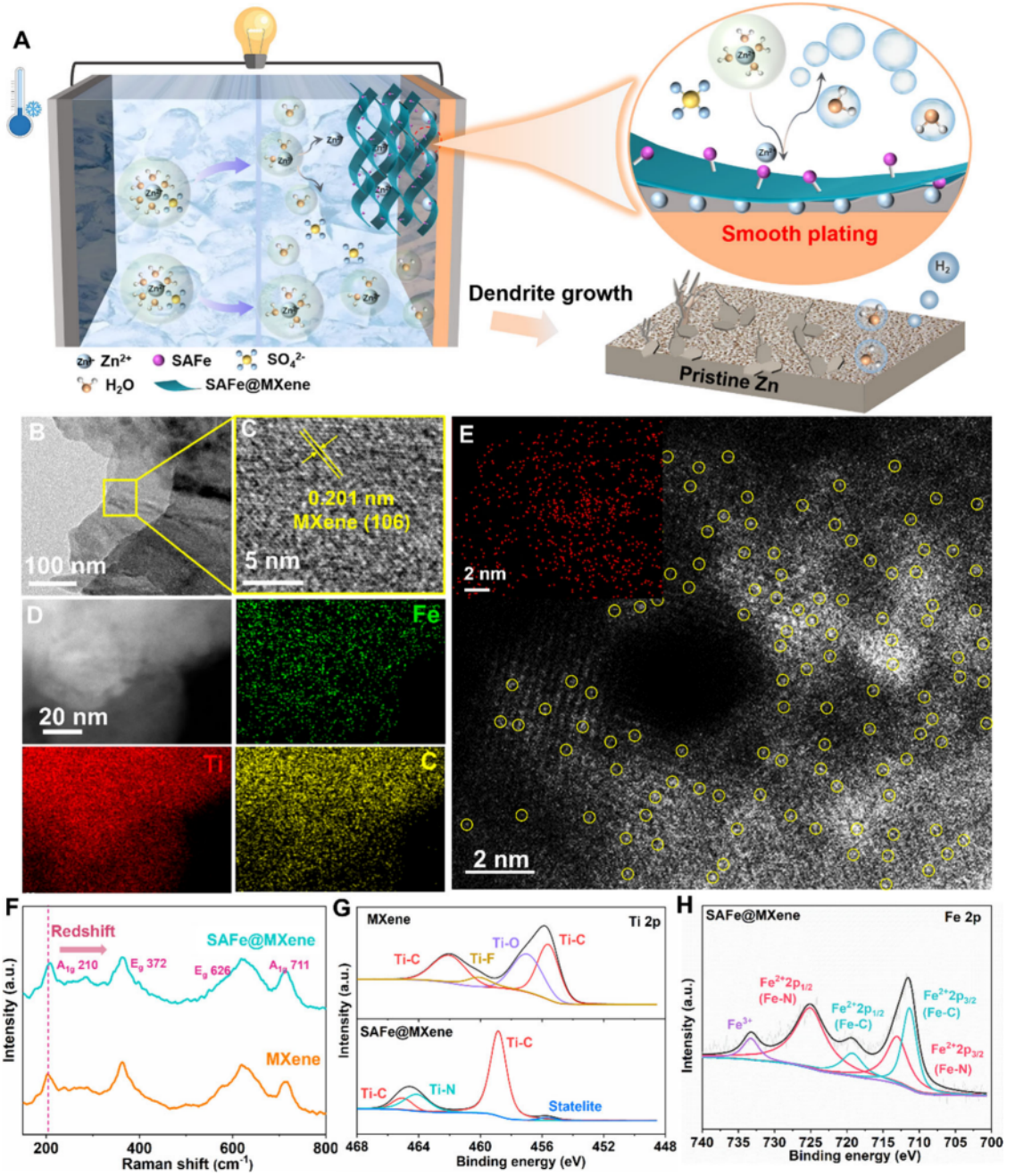


**Figure 1.** Morphology and structural characterizations on the SAFe@MXene nanocatalyst. (A) Schematic illustration of the catalytic SAFe@MXene layer in accelerating desolvation and further promoting smooth Zn plating at the Zn/electrolyte interface; (B) TEM image and (C) HRTEM image of the crumpled SAFe@MXene nanosheets; (D) EDX elemental maps for the SAFe@MXene nanosheets; (E) HAADF-STEM image and an inset showing the corresponding EDX map of elemental Fe distributed in the SAFe@MXene nanosheet; (F) Raman comparisons of SAFe@MXene and MXene nanosheets; high-resolution XPS spectra of (G) Ti 2p regions and (H) Fe 2p region of SAFe@MXene and MXene nanosheets, respectively.

promote the dissociation kinetics of $[Zn(H_2O)_x]^{2+}$ into free $Zn^{2+}$, separating water molecules through an energy-favorable way and accelerating the diffusion kinetics of $Zn^{2+}$. However, it is still a mystery whether it works proficiently as expected in the LT-AZMBs.

To produce more active sites, electron delocalization engineering has emerged and is proposed to modulate electronic density.[53−56] Disturbing the local density may cause the breakup of the original electronic distribution, leading to electronic redistribution. Currently, the strategies of defects, single metal atoms, elemental doping, and heterostructures are feasible to regulate the chemical environment via delocalizing electron orbitals, enhancing adsorption capability, and catalytic sites at the interface.[8,57,58] To increase catalytic efficiency, delocalizing the interface formed by the heteroatom introduction, i.e., metallic single atoms in defects can maximize the capability,[48,59−61] redistributing electronic structure. Under the hybridization of delocalized electron orbitals around the central metallic atoms and the substrates, many active sites with tunable electronic capability are formed on the structure interface to enhance the adsorption affinity to ionic species and electron acceptor/donor abilities to uniformize ion flux. In

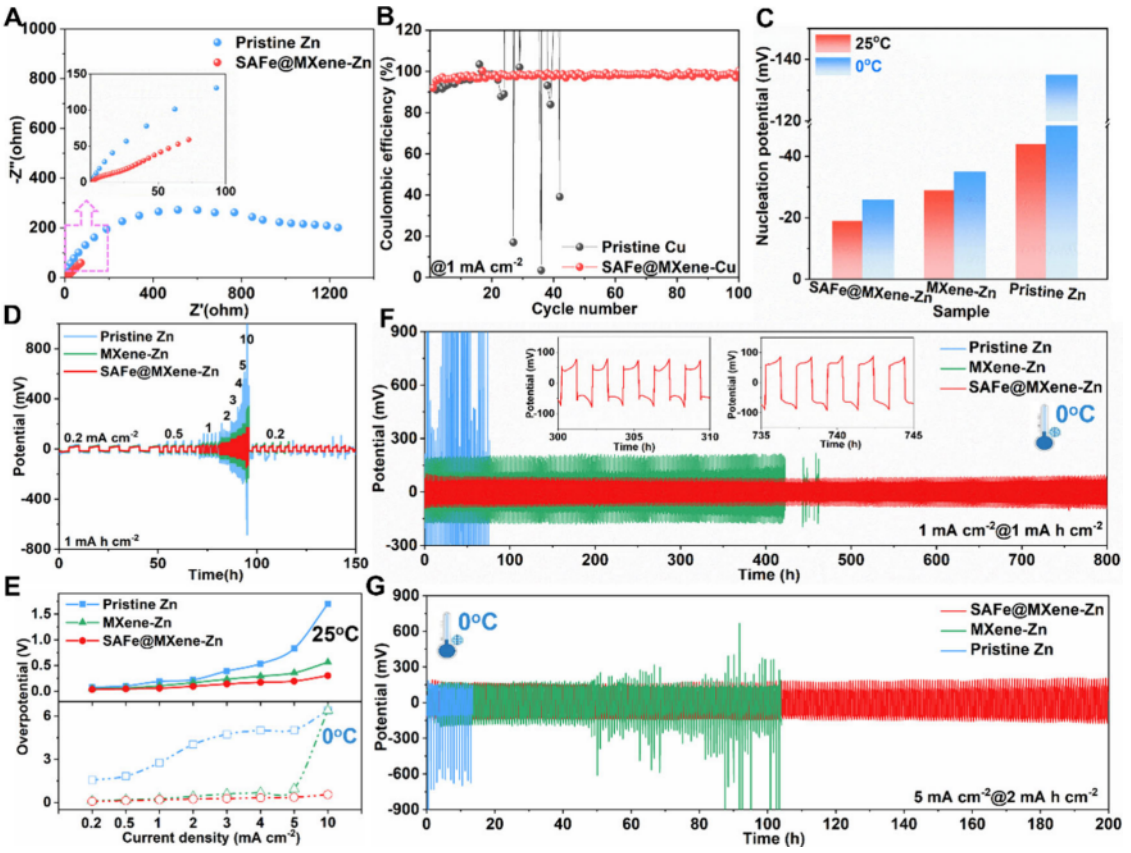


**Figure 2.** Dendrite-free Zn plating performance with the SAFe@MXene catalyst. (A) Comparison of EIS spectra of symmetrical cells based on the different anodes; (B) comparison of Coulombic efficiency tested on SAFe@MXene-Cu and pristine Cu; (C) comparison of Zn nucleation on the SAFe@MXene-Zn, MXene-Zn, and pristine Zn electrodes at 0.2 mA $cm^{-2}$ under room and low temperatures; (D) galvanostatic Zn stripping/plating behaviors from 0.2 to 10 mA $cm^{-2}$ under room temperature; (E) comparison of overpotential gap with shifting current density under room and low temperatures; galvanostatic Zn stripping/plating process (F) at 1 mA $cm^{-2}$ and (G) 5 mA $cm^{-2}$ under the low temperature of 0 °C, respectively.

comparison to artificial layer construction, this emerging catalytic modulation is temperature-insensitive, possessing stronger adaptability to low-temperature operation than conventional electrolyte engineering.[62] MXene, possessing abundant defect sites, has attracted wide attention as a 2D material.[5,63,64] Modifying the hybridization of electron orbitals in the MXene by importing metallic single atoms will cause more interface distortion to increase the number of active sites,[8,48,65,66] leading to fast kinetics of desolvation of $[Zn(H_2O)_x]^{2+}$, $Zn^{2+}$ diffusion, and successive $Zn^0$ lateral deposition. Therefore, it is necessary to develop an electron-delocalization catalyst strategy to satisfy rapid ion/atom exchange with a lower desolvation barrier to further enhance interfacial $Zn^{2+}/Zn^0$ kinetics.

Herein, the kinetics of $Zn^{2+}$ desolvation and diffusion against dendrite growth are promoted by adopting highly active single atomic catalysts (SACs) on MXene and coating on a metallic Zn electrode, which has rarely been reported before. As a prototype in Figure 1A, iron atoms are anchored by defect-rich $Ti_3C_2T_x$ nanosheets (SAFe@MXene), constructing the catalytic modulation layer and providing a catalytic effect. Meanwhile, as illustrated in the optical image and by wettability, the assembled atom-on-MXene also weakens the interaction of $Zn^{2+}$−$H_2O$ bonds with fast desolvation against HER occurrence and dendrite growth simultaneously, as investigated by theoretical simulation, Raman and electrochemical tests. Consequently, the SAFe@MXene-Zn anode enables faster $Zn^{2+}$ nucleation kinetics to achieve an overpotential of 19 mV and long-term stripping/plating lifespan above 1000 h at 2 mA $cm^{-2}$. Even reducing the temperature to 0 °C, the optimized cell maintains reversible stability and lasts for 800 h without any dendrite. The as-prepared SAFe@MXene-Zn full cell coupled with $MnO_2$ displays a high-rate capacity and capacity-retention of nearly 100% at 1.0 A $g^{-1}$ after 1000 cycles, demonstrating the effectiveness of the catalytic modulation layer in inhibiting dendrite formation toward practical LT-AZMBs.

The electron delocalization of SAFe@MXene was prepared by thermolysis and ion-modulation, as detailed in the Supporting Information. As showcased in scanning electron microscopy (SEM) and transmission electron microscopy (TEM), the atomic Fe decorated crumple layered $Ti_3C_2T_x$ (SAFe@MXene) nanosheets (Figure S1) were obtained after the pyrolysis of melamine, and the Fe element was anchored onto defect-rich MXene (Figure S2) with uniform distributions (Figure S3). The TEM images in Figure 1B and S4 show the sheet-like and crumpled structure morphology, illustrating the well-assembled porous channel structure (Figures S4 and S5), which is confirmed by the mesopores ranging from 4 to 50 nm for sieving hydrated $Zn(H_2O)_6^{2+}$ groups to get rid of $H_2O$ to release more free $Zn^{2+}$ (Figure S6). A lattice fringe of 0.201 nm in SAFe@MXene is observed, which is consistent with the (106) crystal plane of MXene (Figure 1B and 1C). Furthermore, the atomic resolution high-angle annular dark-

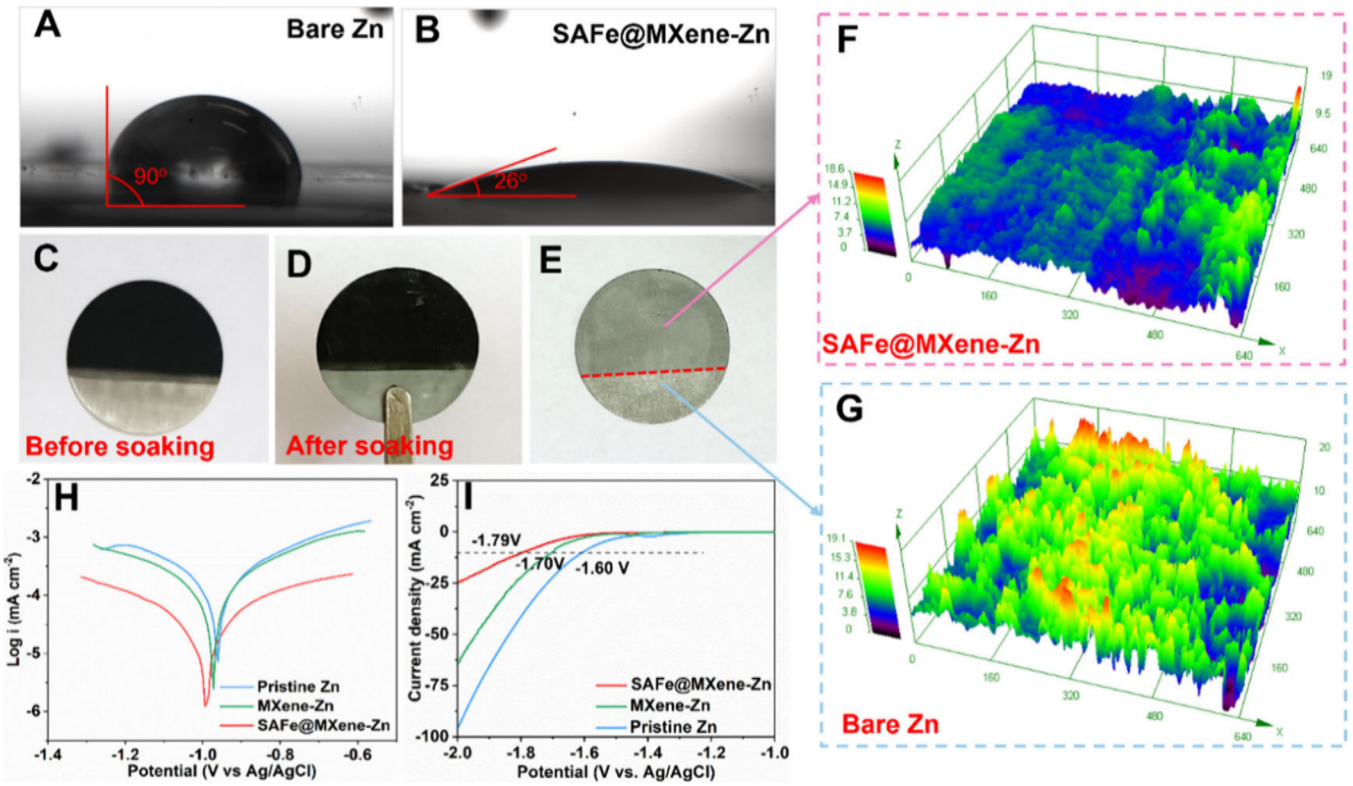


**Figure 3.** Roles of the SAFe@MXene layer on inhibiting active water molecules. Comparison of contact angles of the electrolyte on the surface of (A) bare Zn and (B) SAFe@MXene-Zn; (C) optical images of partially coated SAFe@MXene-Zn (C) before and (D) after electrolyte soaking; (E) Zn image after removing the upper modulation layer; confocal microscopic 3D morphology of the soaked Zn (F) with and (G) without an upper modulation layer; (H) Tafel plots and (I) linear sweep voltammetry (LSV) curves of SAFe@MXene-Zn, MXene-Zn, and bare Zn on a three-electrode system.

field scanning transmission electron microscopy (HAADF-STEM) of the SAFe@MXene reveals the atomic presence. The Fe atoms in the SAFe@MXene nanosheet retains a smooth morphology without any obvious agglomerates (Figure 1D and 1E). Combining the high-resolution HAADF-STEM image with the corresponding elemental dispersed X-ray (EDX) spectrum of Fe mapping (Figures S7 and 1E), the elemental Fe atoms indicated and highlighted by yellow spots on SAFe@MXene are uniformly distributed, demonstrating the successful location of isolated atomic Fe in the defect-rich MXene.

The enlarged interplanar spacing of SAFe@MXene is also confirmed by X-ray diffraction (XRD) in Figure S8. Figure 1F provides the chemical surroundings of the defect-rich MXene before and after introducing a metal atom. Apparently, an observed red-shift of 210 $cm^{-1}$ is created on the $A_{1g}$ (symmetric out-of-plane vibrations) and $E_g$ (in-plane vibrations) vibrations in the SAFe@MXene, confirming that the Fe atomic sites have triggered electronic density redistribution. To further understand the electronic reconstruction, X-ray photoelectron spectroscopy (XPS) was employed to inspect the chemical valence changes (Figures 1G,H and S9). In comparison to the Ti 2p spectrum of MXene (Figure 1G), the introduction of Fe atoms shifts the dominant peak of Ti−C species to 458.8 and 465.1 eV,[64] indicating the reconstruction of electron density states. Meanwhile, the high-resolution Fe 2p XPS spectrum of SAFe@MXene in Figure 1H exhibits Fe−C ($Fe^{2+}$ $2p_{3/2}$: 711.4 eV and $Fe^{2+}$ $2p_{1/2}$: 719.3 eV) and Fe−N ($Fe^{2+}$ $2p_{3/2}$: 713.1 eV and $Fe^{2+}$ $2p_{1/2}$: 725.1 eV) species,[67,68] affirming the formation of C−Fe−N bonds as heteroatomic sites in defect-rich MXene. At the same time, the appearance of an Fe−N bond (398.9 eV) in the N 1s spectrum (Figure S9A) and M−C species (M = Ti and Fe) at 282.2 eV also affirms the existence of C−Fe−N bonds (Figure S9B).[64] Overall, the above results evidently showcase the presence of SAFe in the defect-rich MXene and verify the regulation of intrinsic electronic density for generating more catalytic sites.

Initially, the electrochemical impedance spectroscopy (EIS) of symmetric cells was performed to inspect electron/ion transport kinetics across the interface. The SAFe@MXene-decorated Zn electrode exhibits a decreased charge-transfer resistance ($R_{ct}$) (25 vs 1025 Ω) (Figure 2A) and a smaller $Zn^{2+}$ diffusion resistance than the pristine Zn (Figure S10), implying faster exchange kinetics. Successively, the cycling behaviors of SAFe@MXene-Zn electrodes were evaluated in asymmetric cells and symmetric cells. The Coulombic efficiency value of SAFe@MXene-Cu//Zn cell is evaluated as high as 99.8%, while the pristine Cu only survives for 20 cycles (Figure 2B), indicating the catalytic sieving effect in dissociating $Zn^{2+}$-$H_2O$ by SAFe@MXene. The SAFe@MXene-Zn electrodes present remarkably decreased nucleation barriers at room and low temperatures (Figures 2C and S11). For example, under a low-temperature surrounding of 0 °C, the SAFe@MXene-Zn electrode still obtains the lowest nucleation barrier (26 vs 35 vs 135 mV), indicating the fast desolvation toward $[Zn(H_2O)_x]^{2+}$ clusters. In the successive stripping−plating behaviors, the SAFe@MXene-Zn electrode displays gradually increased voltage hysteresis when the current density increases from 0.2 to 10 mA $cm^{-2}$ (Figures 2D,E and S12). The Zn//Zn symmetric cell experiences increased voltage hysteresis under low temperature or high current density (Figure S12).

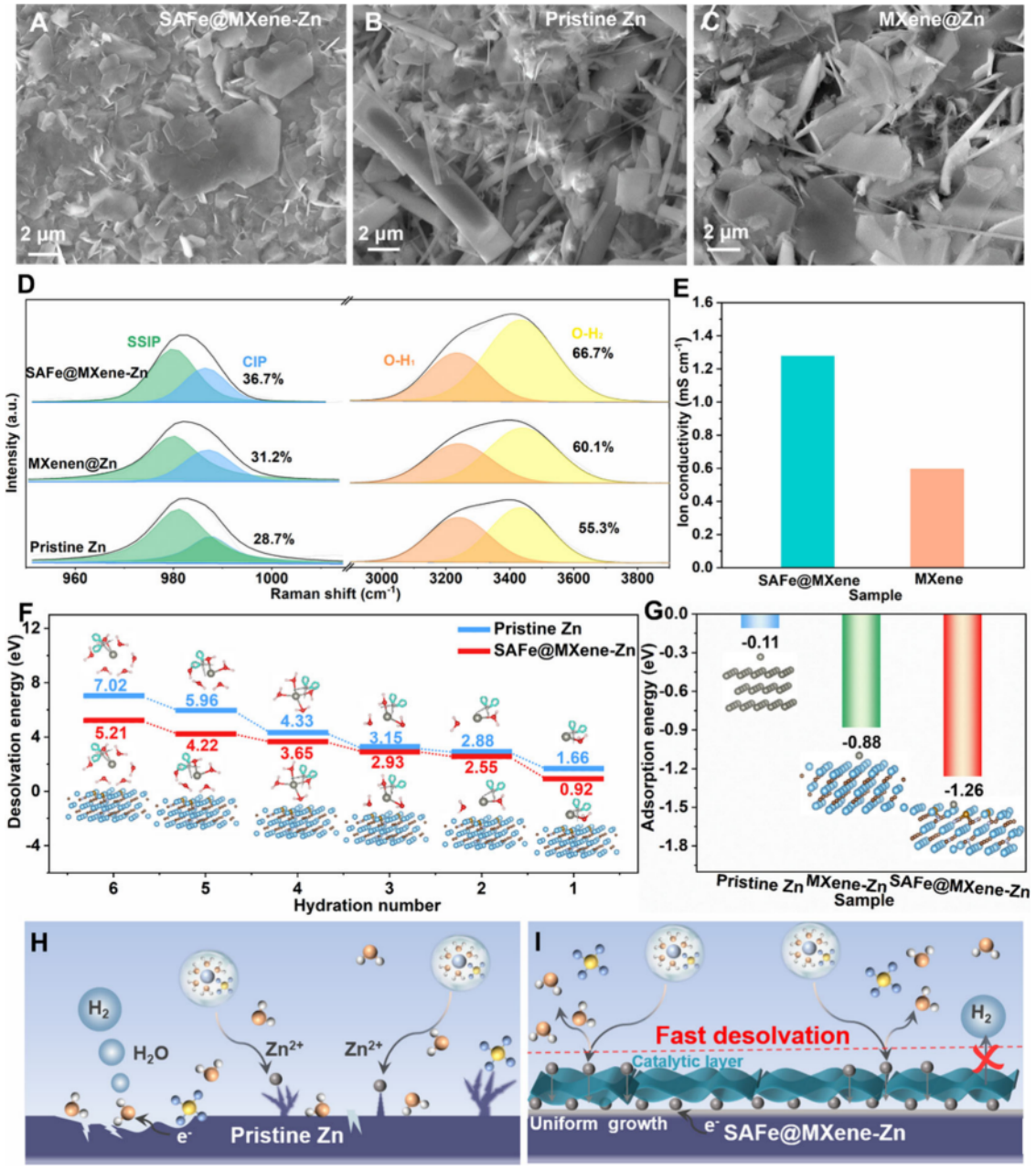


**Figure 4.** Mechanism of SAFe@MXene catalyst in accelerating $Zn^{2+}$ desolvation for lateral Zn electroplating. SEM morphology of the cycled (A) SAFe@MXene-Zn, (B) pristine Zn, and (C) MXene@Zn electrodes after striping/plating; (D) Raman spectra of $\nu$-$SO_4^{2-}$ and O−H bonds at different electrode/electrolyte interfaces; (E) ionic conductivity test at the interface of SAFe@MXene-Zn/electrolyte and MXene-Zn/electrolyte; (F) comparison of $[Zn(H_2O)_6]^{2+}$ desolvation barriers with/without SAFe@MXene; (G) adsorption energies of Zn atoms on three different surfaces; schematic illustrations of (H) dendrite growth and HER on pristine Zn and (I) synergistic desolvation mechanism of catalysis with porous sieving from the SAFe@MXene nanosheets avoiding side reactions and dendrite growth.

However, the overpotentials of a symmetric cell with SAFe@MXene-Zn are 80, 239, 356, and 545 mV at 0.2, 2, 5, and 10 mA $cm^{-2}$ (Figure 2E), respectively, much lower than those of bare Zn. To verify the electroplating stability, the SAFe@MXene-modulated Zn anode is stabilized for 200 h with a small overpotential around 76 mV at 0.5 mA $cm^{-2}$, while the pristine Zn is suddenly short-circuited after merely 70 h with an overpotential larger than 1200 mV, exhibiting severe side reactions and dendrite growth (Figure S13). Increasing to 2 mA $cm^{-2}$ (2 mA h $cm^{-2}$) in Figure S14, the SAFe@MXene-Zn electrode retains an outstanding cycling life over 1000 h, which is 5 times longer than that of a bare Zn electrode.

Decreasing the operation temperature to 0 °C, the solvated $[Zn(H_2O)_x]^{2+}$ clusters usually get larger and face higher barriers owing to the significantly increased steric hindrance from expansion of the hydrogen bond networks as freezing solidification of the electrolyte (Figure S15).[1,16,29,30] The SAFe@MXene-Zn electrode can achieve a cycling life of 800 h and stabilize the overpotential around 170 mV at 1 mA $cm^{-2}$ (Figure 2F). Even increasing to 5 mA $cm^{-2}$ and 2 mA h $cm^{-2}$ simultaneously, the SAFe@MXene-Zn electrode stabilizes the overpotential of 350 mV within 200 h, while dendrite growth is observed on the MXene-Zn electrode over 100 h (Figure 2G),

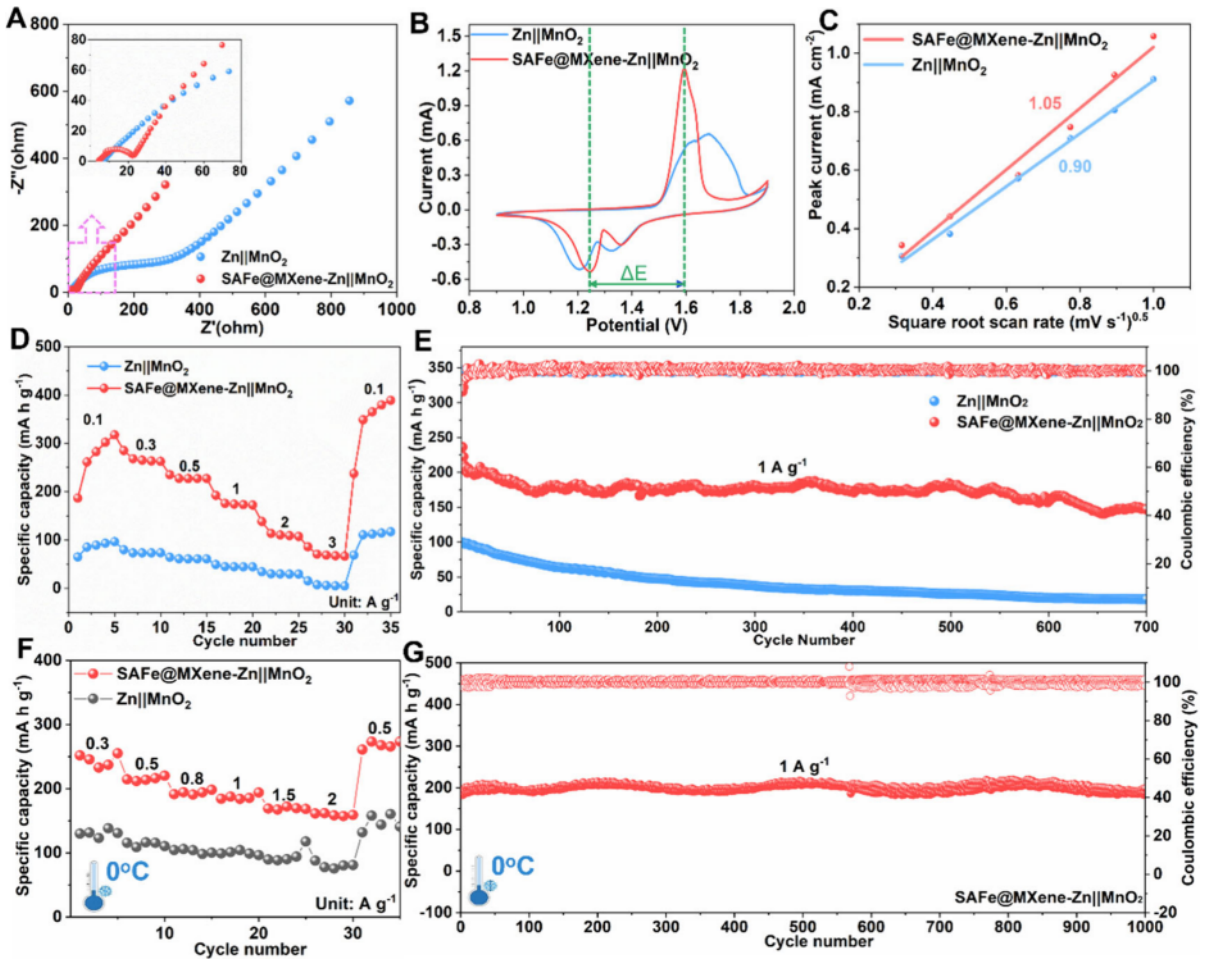


**Figure 5.** Electrochemical performance of full batteries based on the SAFe@MXene-Zn anode. (A) EIS spectra and (B) CV curves at 0.1 mV $s^{-1}$ for full cells based on pristine Zn and SAFe@MXene-Zn anodes; (C) plots of the peak current density recorded at the anodic current peak versus the square root of the scan rates; (D) rate performance of the full cells based on pristine Zn and SAFe@MXene-Zn electrodes; (E) comparison of long-term cycle stability of the two full cells; (F) comparison of rate performance under a low temperature of 0 °C; (G) long-term cycle stability of the SAFe@MXene-Zn//$MnO_2$ full cell under a low temperature of 0 °C.

further implying the atomic catalytic effect on promoting $Zn^{2+}$ desolvation and diffusion.

As known, poor interfacial wettability will undoubtedly lead to slow kinetics of $Zn^{2+}$ diffusion due to the huge impedance. Reducing the content of active water molecules in the solvation shell would be beneficial to enhance the desolvation of hydrated $Zn^{2+}$ and reduce the diffusion space resistance of $Zn^{2+}$as well as the occurrence of HER. Figures 3A,B and S16 display the contact angle of the electrolyte on the different electrodes, and bare Zn foil (90°) displays poor hydrophilicity compared with MXene-Zn (52°) and SAFe@MXene-Zn (26°), suggesting the zincophilic nature of atomic catalytic sites (Figure 3B).[38,41] Under natural soaking for 3 weeks (Figure 3C−G), the Zn electrode after removing the SAFe@MXene modulation layer still maintains a significantly smooth surface without obvious corrosion (Figure 3E and 3F). In sharp contrast, a much coarser surface with severe corrosion morphology is formed on the bare Zn electrode (Figure 3E and 3G), suggesting the occurrence of possible severe side reactions.

To further verify the anticorrosion effect, the Tafel curve was recorded and a decreased corrosion current from $1.81 \times 10^{-4}$ to $2.95 \times 10^{-5}$ mA $cm^{-2}$ with SAFe@MXene-Zn was depicted (Figures 3H and S17). Also, the anti-HER capability of the SAFe@MXene-Zn layer was compared (Figure 3I). The decoration of SAFe@MXene dramatically decreases the current density and extends the HER potential from −1.60 to −1.79 V at 10 mA $cm^{-2}$, demonstrating the prohibition of the HER via fast desolvation kinetics. Moreover, the roughly estimated thickness of the coin cell with an SAFe@MXene modulation layer increases the least without electrolyte leakage after several repeated Zn stripping/plating behaviors (Figures S18 and S19), additionally proving the inhibition of the SAFe@MXene on HER at the interface. These results suggest the remarkably improved corrosion resistance to the electrolyte of the zinc electrode and well-restrained hydrogen evolution reaction with the SAFe@MXene modulation layer.

To directly observe the optimization on Zn plating, the surface morphologies of cycled Zn electrodes with/without SAFe@MXene were inspected by SEM. As shown in Figure 4A, the surface of the Zn anode with SAFe@MXene modulators remains flat and has a smooth deposition. The presented microflakes are attributed to the typical hexagon crystalline grains on the Zn (002) plane instead of any other substance, which is verified by XRD of the cycled SAFe@MXene-Zn (Figure S20).[6,8,69] However, large amounts of needle-like Zn dendrites appear on the bare Zn anode (Figure 4B) as well as a dendrite deposition trend on the MXene-Zn

anode (Figure 4C). Obviously, the generated Zn atoms are capable of penetrating through the catalytic layer and reaching the bottom Zn metal, which is consistent with our SEM results. Thanks to the improved catalytic capability of the assembled SAFe@MXene layer, the energy barriers for $Zn^{2+}$ desolvation and interfacial $Zn^{2+}$ transfer are obviously decreased to prevent side reactions and dendrite formation. As is known, the desolvation behavior takes place at the electrode/electrolyte interface, and the enhanced kinetics of $[Zn(H_2O)_6]^{2+}$ desolvation is also proved by Raman spectra of $\nu$-$SO_4^{2-}$ and the O−H bond vibration. Two types of ion-pair species of solvent-separated ion pairs (SSIP, $[Zn^{2+}(H_2O)_6{\cdot}OSO_3^{2-}]$) and contact ion pairs (CIP, $[Zn^{2+}(H_2O)_5{\cdot}OSO_3^{2-}]$) can be separated. As illustrated in Figure 4D, with the electron delocalization by SAFe, the percentage of CIP in SAFe@MXene progressively increases (36.7% vs 31.2% vs 28.7%), indicating the SAFe@MXene layer is capable of squeezing out more solvent molecules. Alternatively, the variation trend of the O−H stretch vibration is divided into two peaks, namely, a robust hydrogen bond (O−$H_1$) within 3100−3400 $cm^{-1}$ and a weaker hydrogen bond (O−$H_2$) within 3300−3800 $cm^{-1}$. A repressed stretch peak of O−$H_1$ with the SAFe@MXene catalysis layer is found, corresponding to a larger stretch of O−$H_2$ (66.7%) than that at the unmodulated Zn/electrolyte interface (55.3%). As a result, the corresponding Zn ion conductivity ($\sigma$) of the SAFe@MXene layer is markedly increased to 1.27 mS $cm^{-1}$, 2.2 times greater than that for the MXene layer (Figures 4E and S21), which is comparable to or even better than the reported coatings (Table S1). Altogether, the electrochemical measurements, spectral measurement, and theoretical simulation comprehensively demonstrate the facilitated desolvation kinetics accelerated by SAFe@MXene.

To elaborate the desolvation process of $[Zn(H_2O)_x]^{2+}$ at the electrode/electrolyte interface, density functional theory (DFT) calculations were performed (Figure 4F). In each desolvation step, the dissociation of $[Zn(H_2O)_x]^{2+}$ at the SAFe@MXene-Zn/electrolyte interface costs less energy than that at the pristine Zn/electrolyte interface. For example, $[Zn(H_2O)_6]^{2+}$ at the SAFe@MXene-Zn/electrolyte interface requires merely 5.21 eV to completely release the water solvent, while as high as 7.02 eV is necessary for the pristine Zn/electrolyte interface. As is known, the high affinity between the Zn atom and electrode surface can also effectively boost the desolvation of $[Zn(H_2O)_6]^{2+}$ and delocalize the Zn atom plating. A higher adsorption preference (−1.26 eV) on the SAFe@MXene layer is achieved in comparison to those of MXene-Zn (−0.88 eV) and pristine Zn (−0.11 eV) (Figure 4G), further verifying the contribution of the SAFe@MXene layer to promote $Zn^{2+}$ desolvation. In detailed elaboration, in comparison with severe side reactions of HER (Figure 4H), the electron delocalization artificial layer (SAFe@MXene) serves as the functional catalytic layer to prevent the active water in the hydrated $[Zn(H_2O)_x]^{2+}$ to come into the HER. When the SAFe@MXene nanosheets are developed as the catalytic SEI layer for the Zn anode (Figure 4I), the active water molecules are dissociated to extend the HER potential, regulating the desolvation and $Zn^{2+}$ transfer behaviors.

To explore the practical application of the SAFe@MXene-Zn anode, a full cell employing $MnO_2$ shows a dramatically decreased $R_{ct}$ (20 vs 293 Ω) and higher diffusion kinetics than the control one (Figures 5A and S22). The two pairs of redox peaks occur with a reduced voltage gap (0.34 vs 0.42 V), and the good overlapping reflects excellent reversibility with the help of the SAFe@MXene catalyst (Figures 5B and S23). On gradually increasing to 1 mV $s^{-1}$, SAFe@MXene-Zn presents higher Zn ion diffusion kinetics with a larger linear slope recorded on the oxidation peaks (1.05 vs 0.90) (Figures 5C and S24). Consequently, the optimized full cell exhibits a weaker voltage hysteresis of 190 mV (Figure S25) and superior rate capacities of 140 and 88 mA h $g^{-1}$ at 2 and 3 C, respectively, significantly higher than that of the control ones (37 and 17 mA h $g^{-1}$) (Figures 5D and S26). As is wellknown, the capacity of a full cell is related to the thermodynamic and electrochemical kinetics of $Zn^{2+}$, and both the full cells based on SAFe@MXene-Zn and the pristine Zn anode present a comparable capacity at 0.05 A $g^{-1}$ (Figure S27). The SAFe@MXene-modified full cell stabilizes at 148 mA h $g^{-1}$ after 700 cycles with a capacity decay rate as low as 0.053% per cycle at 1.0 A $g^{-1}$ (Figure 5E). In sharp contrast, the pristine Zn one sharply degrades to near failure at around 15 mA h $g^{-1}$ after 700 cycles. On decreasing to 0 °C, the SAFe@MXene-Zn-based cell still delivers an excellent rate performance of 252 mA h $g^{-1}$ even at 0.3 A $g^{-1}$, which maintains 161 mA h $g^{-1}$ at 2 A $g^{-1}$, whereas the pristine Zn//$MnO_2$ cell decreases to merely 87 mA h $g^{-1}$ (Figure 5F). Moreover, the cell with an SAFe@MXene-Zn anode still delivers a high specific capacity of 193 mA h $g^{-1}$ and stabilizes at 198 mA h $g^{-1}$ with a high capacity-retention of nearly 100% at 1 A $g^{-1}$ after 1000 cycles due to inhibited dissolution of $Mn^{2+}$ into the electrolyte under the low-temperature effect (Figure 5G), demonstrating superior low-temperature operation potential to those reported in recent literature (Table S2).

In summary, an electron redistribution strategy through implanting atomic Fe into defect-rich MXene (SAFe@MXene) is proposed as a catalytic layer, where the increased catalytic sites enable lower barriers of interfacial dissociation of $[Zn(H_2O)_x]^{2+}$ to release affluent free $Zn^{2+}$, as revealed by theoretical and electrochemical tests. Also, the sieving channels assembled by crumpled SAFe@MXene nanosheets can strengthen the sieving effect toward dissociating $[Zn(H_2O)_x]^{2+}$. Consequently, under 0 °C, a long-term life of 800 h at 1 mA $cm^{-2}$ with very stable overpotential is achieved and low overpotentials even at a high current density of 5 mA $cm^{-2}$ or under high plating/stripping capacity are still retained. The full cell delivers stability at 198 mA h $g^{-1}$ after 1000 cycles with a high capacity-retention of 100% at 1.0 A $g^{-1}$, shedding new insights to propel desolvation and diffusion kinetics for achieving LT-AZMBs under electron-delocalized engineering.

## AUTHOR INFORMATION


### Corresponding Authors

**Jing Zhang** − *School of Materials Science and Engineering, Xi'an University of Technology, Xi'an 710048, China*; Email: zhangjing2020@xaut.edu.cn

**Caiyin You** − *School of Materials Science and Engineering, Xi'an University of Technology, Xi'an 710048, China*; Email: caiyinyou@xaut.edu.cn

**Hongzhen Lin** − *i-Lab & CAS Key Laboratory of Nanophotonic Materials and Devices, Suzhou Institute of Nano-Tech and Nano-Bionics, Chinese Academy of Sciences, Suzhou 215123, China*; Email: hzlin2010@sinano.ac.cn

**Jian Wang** − *i-Lab & CAS Key Laboratory of Nanophotonic Materials and Devices, Suzhou Institute of Nano-Tech and Nano-Bionics, Chinese Academy of Sciences, Suzhou 215123, China; Helmholtz Institute Ulm (HIU), Ulm D89081, Germany; Karlsruhe Institute of Technology, Karlsruhe D76021, Germany*; orcid.org/0000-0002-7945-0826; Email: jian.wang@kit.edu, wangjian2014@sinano.ac.cn

## Authors

**Lu Pan** − *School of Materials Science and Engineering, Xi'an University of Technology, Xi'an 710048, China*

**Lujie Jia** − *i-Lab & CAS Key Laboratory of Nanophotonic Materials and Devices, Suzhou Institute of Nano-Tech and Nano-Bionics, Chinese Academy of Sciences, Suzhou 215123, China*

**Jing Dong** − *i-Lab & CAS Key Laboratory of Nanophotonic Materials and Devices, Suzhou Institute of Nano-Tech and Nano-Bionics, Chinese Academy of Sciences, Suzhou 215123, China*

**Chenxiao Han** − *School of Materials Science and Engineering, Xi'an University of Technology, Xi'an 710048, China*

**Na Tian** − *School of Materials Science and Engineering, Xi'an University of Technology, Xi'an 710048, China*

**Xiaomin Cheng** − *i-Lab & CAS Key Laboratory of Nanophotonic Materials and Devices, Suzhou Institute of Nano-Tech and Nano-Bionics, Chinese Academy of Sciences, Suzhou 215123, China*

**Bingbing Tang** − *i-Lab & CAS Key Laboratory of Nanophotonic Materials and Devices, Suzhou Institute of Nano-Tech and Nano-Bionics, Chinese Academy of Sciences, Suzhou 215123, China*

**Qinghua Guan** − *i-Lab & CAS Key Laboratory of Nanophotonic Materials and Devices, Suzhou Institute of Nano-Tech and Nano-Bionics, Chinese Academy of Sciences, Suzhou 215123, China*

**Yongzheng Zhang** − *State Key Laboratory of Chemical Engineering, East China University of Science and Technology, Shanghai 200237, China*; orcid.org/0000-0003-3889-1710

**Bo Deng** − *School of Materials Science and Engineering, Xi'an University of Technology, Xi'an 710048, China*

**Li Lei** − *School of Materials Science and Engineering, Xi'an University of Technology, Xi'an 710048, China*; orcid.org/0000-0003-3142-4095

**Meinan Liu** − *i-Lab & CAS Key Laboratory of Nanophotonic Materials and Devices, Suzhou Institute of Nano-Tech and Nano-Bionics, Chinese Academy of Sciences, Suzhou 215123, China*; orcid.org/0000-0003-2552-1091

## Notes

The authors declare no competing financial interest.

## ■ ACKNOWLEDGMENTS

The authors acknowledge financial support from the National Key R&D Program of China (2021YFA1201503), the National Natural Science Foundation of China (Nos. 22309144, 52371198, 52171191, 21972164, 22279161), the Natural Science Foundation of Jiangsu Province (BK. 20210130), Suzhou Science and Technology Plan projects (SYC2022057), Opening funding from Key Laboratory of Engineering Dielectrics and Its Application (Harbin University of Science and Technology) (No. KFM202507, Ministry of Education), China Postdoctoral Science Foundation (Nos. 2023M732561, 2023M731084, 2024M762318), Shanghai Sailing Program of China (23YF1408900), and Scientific Research Program of Shaanxi Provincial Education Department (No. 21JP083). J. Wang thanks the fellowship support provided by the Alexander von Humboldt Foundation. Y. Zhang thanks the Shanghai Super Postdoctoral Incentive Program. The authors are also grateful for the technical support from Nano-X, Suzhou Institute of Nanotech and Nanobionics, Chinese Academy of Sciences, and Advanced Material Analysis and Test Center of Xi'an University of Technology.

## ■ REFERENCES

(1) Han, M.; Li, T. C.; Chen, X.; Yang, H. Y. Electrolyte Modulation Strategies for Low-Temperature Zn Batteries. *Small* **2024**, *20* (3), 202304901.

(2) Liao, M.; Wang, J.; Ye, L.; Sun, H.; Wen, Y.; Wang, C.; Sun, X.; Wang, B.; Peng, H. A Deep-Cycle Aqueous Zinc-Ion Battery Containing an Oxygen-Deficient Vanadium Oxide Cathode. *Angew. Chem., Int. Ed.* **2020**, *59* (6), 2273−2278.

(3) Wang, W.; Chen, S.; Liao, X.; Huang, R.; Wang, F.; Chen, J.; Wang, Y.; Wang, F.; Wang, H. Regulating Interfacial Reaction through Electrolyte Chemistry Enables Gradient Interphase for Low-Temperature Zinc Metal Batteries. *Nat. Commun.* **2023**, *14* (1), 5443.

(4) Meng, J.; Song, Y.; Qin, Z.; Wang, Z.; Mu, X.; Wang, J.; Liu, X. X. Cobalt-Nickel Double Hydroxide toward Mild Aqueous Zinc-Ion Batteries. *Adv. Funct. Mater.* **2022**, *32* (33), 2204026.

(5) Zhang, Y.; Cao, Z.; Liu, S.; Du, Z.; Cui, Y.; Gu, J.; Shi, Y.; Li, B.; Yang, S. Charge-Enriched Strategy Based on Mxene-Based Polypyrrole Layers toward Dendrite-Free Zinc Metal Anodes. *Adv. Energy Mater.* **2022**, *12* (13), 2103979.

(6) Zheng, Z.; Zhong, X.; Zhang, Q.; Zhang, M.; Dai, L.; Xiao, X.; Xu, J.; Jiao, M.; Wang, B.; Li, H.; Jia, Y.; Mao, R.; Zhou, G. An Extended Substrate Screening Strategy Enabling a Low Lattice Mismatch for Highly Reversible Zinc Anodes. *Nat. Commun.* **2024**, *15* (1), 753.

(7) Cheng, X.; Zuo, Y.; Zhang, Y.; Zhao, X.; Jia, L.; Zhang, J.; Li, X.; Wu, Z.; Wang, J.; Lin, H. Superfast Zincophilic Ion Conductor Enables Rapid Interfacial Desolvation Kinetics for Low-Temperature Zinc Metal Batteries. *Adv. Sci.* **2024**, *11* (28), 2401629.

(8) Chen, S.; Chen, J.; Liao, X.; Li, Y.; Wang, W.; Huang, R.; Zhao, T.; Yan, S.; Yan, Z.; Cheng, F.; Wang, H. Enabling Low-Temperature and High-Rate Zn Metal Batteries by Activating Zn Nucleation with Single-Atomic Sites. *ACS Energy Lett.* **2022**, *7* (11), 4028−4035.

(9) Wang, Y.; Fan, Y.; Liao, D.; Wu, Y.; Yu, Y.; Hu, C. Highly $Zn^{2+}$-Conductive and Robust Modified Montmorillonite Protective Layer of Electrodes toward High-Performance Rechargeable Zinc-Ion Batteries. *Energy Storage Mater.* **2022**, *51*, 212−222.

(10) Cao, Z.; Du, Z.; Jia, K.; Jin, L.; Li, N.; Zhang, M.; Zao, R.; Abdelkader, A.; Kumar, R. V.; Ding, S.; Xi, K.; Yang, S. Bubbling Chemical Vapors in Molten Metal toward XIV-Group Nanosheets. *Nano Lett.* **2024**, *24* (46), 14559−14566.

(11) Liu, S.; Zhang, R.; Mao, J.; Zhao, Y.; Cai, Q.; Guo, Z. From Room Temperature to Harsh Temperature Applications: Fundamentals and Perspectives on Electrolytes in Zinc Metal Batteries. *Sci. Adv.* **2022**, *8* (12), 5079.

(12) Chu, Y.; Zhang, S.; Wu, S.; Hu, Z.; Cui, G.; Luo, J. In Situ Built Interphase with High Interface Energy and Fast Kinetics for High Performance Zn Metal Anodes. *Energy Environ. Sci.* **2021**, *14* (6), 3609−3620.

(13) (13) Bai, S.; Huang, Z.; Liang, G.; Yang, R.; Liu, D.; Wen, W.; Jin, X.; Zhi, C.; Wang, X. Electrolyte Additives for Stable Zn Anodes. *Adv. Sci.* **2024**, *11* (4), 2304549.
(14) Chang, Z.; Yang, H.; Qiao, Y.; Zhu, X.; He, P.; Zhou, H. Tailoring the Solvation Sheath of Cations by Constructing Electrode Front-Faces for Rechargeable Batteries. *Adv. Mater.* **2022**, *34* (34), No. e2201339.
(15) Hou, Z.; Lu, Z.; Chen, Q.; Zhang, B. Realizing Wide-Temperature Zn Metal Anodes through Concurrent Interface Stability Regulation and Solvation Structure Modulation. *Energy Storage Mater.* **2021**, *42*, 517−525.
(16) Qiu, Y.; Zheng, X.; Zhang, R.; Lin, Q.; Li, M.; Luo, J.; Yang, S.; Liu, Z.; Wang, Q.; Yu, Y.; Yang, C. Boosting Zinc-Ion Batteries with Innovative Ternary Electrolyte for Enhanced Interfacial Electrochemistry and Temperature-Resilient Performance. *Adv. Funct. Mater.* **2024**, *34* (4), 2310825.
(17) Wang, J.; Zhu, Q.; Li, F.; Chen, J.; Yuan, H.; Li, Y.; Hu, P.; Kurbanov, M. S.; Wang, H. Low-Temperature and High-Rate Zn Metal Batteries Enabled by Mitigating $Zn^{2+}$ Concentration Polarization. *Chem. Eng. J.* **2022**, *433*, 134589.
(18) Li, G.; Zhao, Z.; Zhang, S.; Sun, L.; Li, M.; Yuwono, J. A.; Mao, J.; Hao, J.; Vongsvivut, J.; Xing, L.; Zhao, C.-X.; Guo, Z. A Biocompatible Electrolyte Enables Highly Reversible Zn Anode for Zinc Ion Battery. *Nat. Commun.* **2023**, *14* (1), 6526.
(19) Yan, H.; Li, S.; Nan, Y.; Yang, S.; Li, B. Ultrafast Zinc-Ion-Conductor Interface toward High-Rate and Stable Zinc Metal Batteries. *Adv. Energy Mater.* **2021**, *11* (18), 2100186.
(20) Liu, Z.; Luo, X.; Qin, L.; Fang, G.; Liang, S. Progress and Prospect of Low-Temperature Zinc Metal Batteries. *Adv. Powder Mater.* **2022**, *1* (2), 100011.
(21) Wang, R.; Ma, Q.; Zhang, L.; Liu, Z.; Wan, J.; Mao, J.; Li, H.; Zhang, S.; Hao, J.; Zhang, L.; Zhang, C. An Aqueous Electrolyte Regulator for Highly Stable Zinc Anode under −35 to 65 °C. *Adv. Energy Mater.* **2023**, *13* (40), 2302543.
(22) Wang, Z.; Huang, J.; Guo, Z.; Dong, X.; Liu, Y.; Wang, Y.; Xia, Y. A Metal-Organic Framework Host for Highly Reversible Dendrite-Free Zinc Metal Anodes. *Joule* **2019**, *3* (5), 1289−1300.
(23) Hu, Y.; Fu, C.; Chai, S.; He, Q.; Wang, Y.; Feng, M.; Zhang, Y.; Pan, A. Construction of Zinc Metal-Tin Sulfide Polarized Interface for Stable Zn Metal Batteries. *Adv. Powder Mater.* **2023**, *2* (2), 100093.
(24) Zong, Q.; Lv, B.; Liu, C.; Yu, Y.; Kang, Q.; Li, D.; Zhu, Z.; Tao, D.; Zhang, J.; Wang, J.; Zhang, Q.; Cao, G. Dendrite-Free and Highly Stable Zn Metal Anode with $BaTiO_3$/P(VDF-TrFE) Coating. *ACS Energy Lett.* **2023**, *8* (7), 2886−2896.
(25) Zeng, X.; Mao, J.; Hao, J.; Liu, J.; Liu, S.; Wang, Z.; Wang, Y.; Zhang, S.; Zheng, T.; Liu, J.; Rao, P.; Guo, Z. Electrolyte Design for In Situ Construction of Highly $Zn^{2+}$-Conductive Solid Electrolyte Interphase to Enable High-Performance Aqueous Zn-Ion Batteries under Practical Conditions. *Adv. Mater.* **2021**, *33* (11), 2007416.
(26) Wang, J.; Yang, J.; Xiao, Q.; Zhang, J.; Li, T.; Jia, L.; Wang, Z.; Cheng, S.; Li, L.; Liu, M.; Liu, H.; Lin, H.; Zhang, Y. In Situ Self-Assembly of Ordered Organic/Inorganic Dual-Layered Interphase for Achieving Long-Life Dendrite-Free Li Metal Anodes in LiFSI-Based Electrolyte. *Adv. Funct. Mater.* **2021**, *31* (7), 2007434.
(27) Yan, K.; Fan, Y.; Hu, F.; Li, G.; Yang, X.; Wang, X.; Li, X.; Peng, C.; Wang, W.; Fan, H.; Ma, L. A "Polymer-in-Salt" Solid Electrolyte Enabled by Fast Phase Transition Route for Stable Zn Batteries. *Adv. Funct. Mater.* **2024**, *34* (2), 2307740.
(28) Zhu, F.; Wang, J.; Zhang, Y.; Tu, H.; Xia, X.; Zhang, J.; He, H.; Lin, H.; Liu, M. Low-Temperature Lithium Metal Batteries Achieved by Synergistically Enhanced Screening $Li^+$ Desolvation Kinetics. *Adv. Mater.* **2025**, *37*, 2411601.
(29) Zhao, M.; Rong, J.; Huo, F.; Lv, Y.; Yue, B.; Xiao, Y.; Chen, Y.; Hou, G.; Qiu, J.; Chen, S. Semi-Immobilized Ionic Liquid Regulator with Fast Kinetics toward Highly Stable Zinc Anode under −35 to 60 °C. *Adv. Mater.* **2022**, *34* (32), No. e2203153.
(30) Zhang, Q.; Ma, Y.; Lu, Y.; Li, L.; Wan, F.; Zhang, K.; Chen, J. Modulating Electrolyte Structure for Ultralow Temperature Aqueous Zinc Batteries. *Nat. Commun.* **2020**, *11* (1), 4463.
(31) Chen, J.; Wang, Y.; Tian, Z.; Zhao, J.; Ma, Y.; Alshareef, H. N. Recent Developments in Three-Dimensional Zn Metal Anodes for Battery Applications. *InfoMat* **2024**, *6* (1), No. e12485.
(32) Ma, C.; Wang, X.; Lu, W.; Wang, C.; Yue, H.; Sun, G.; Zhang, D.; Du, F. Achieving Stable Zn Metal Anode via a Simple NiCo Layered Double Hydroxides Artificial Coating for High Performance Aqueous Zn-Ion Batteries. *Chem. Eng. J.* **2022**, *429*, 132576.
(33) Wang, T.; Xi, Q.; Li, Y.; Fu, H.; Hua, Y.; Shankar, E. G.; Kakarla, A. K.; Yu, J. S. Regulating Dendrite-Free Zinc Deposition by Red Phosphorous-Derived Artificial Protective Layer for Zinc Metal Batteries. *Adv. Sci.* **2022**, *9* (18), 2200155.
(34) Yang, Y.; Liu, C.; Lv, Z.; Yang, H.; Cheng, X.; Zhang, S.; Ye, M.; Zhang, Y.; Chen, L.; Zhao, J.; Li, C. C. Redistributing Zn-ion Flux by Interlayer Ion channels in Mg-Al Layered Double Hydroxide-Based Artificial Solid Electrolyte Interface for Ultra-Stable and Dendrite-Free Zn Metal Anodes. *Energy Storage Mater.* **2021**, *41*, 230−239.
(35) Zheng, X.; Ahmad, T.; Chen, W. Challenges and Strategies on Zn Electrodeposition for Stable Zn-Ion Batteries. *Energy Storage Mater.* **2021**, *39*, 365−394.
(36) Xu, W.; Li, J.; Liao, X.; Zhang, L.; Zhang, X.; Liu, C.; Amine, K.; Zhao, K.; Lu, J. Fluoride-Rich, Organic-Inorganic Gradient Interphase Enabled by Sacrificial Solvation Shells for Reversible Zinc Metal Batteries. *J. Am. Chem. Soc.* **2023**, *145* (41), 22456−22465.
(37) (37) Xin, W.; Xiao, J.; Li, J.; Zhang, L.; Peng, H.; Yan, Z.; Zhu, Z. Metal-Organic Frameworks with Carboxyl Functionalized Channels as Multifunctional Ion-Conductive Interphase for Highly Reversible Zn Anode. *Energy Storage Mater.* **2023**, *56*, 76−86.
(38) Wang, T.; Wang, P.; Pan, L.; He, Z.; Dai, L.; Wang, L.; Liu, S.; Jun, S. C.; Lu, B.; Liang, S.; Zhou, J. Stabling Zinc Metal Anode with Polydopamine Regulation through Dual Effects of Fast Desolvation and Ion Confinement. *Adv. Energy Mater.* **2023**, *13* (5), 2203523.
(39) Cao, J.; Sun, Y.; Zhang, D.; Luo, D.; Zhang, L.; Chanajaree, R.; Qin, J.; Yang, X.; Lu, J. Interfacial Double-Coordination Effect Guiding Uniform Electrodeposition for Reversible Zinc Metal Anode. *Adv. Energy Mater.* **2024**, *14* (2), 2302770.
(40) Zheng, J.; Cao, Z.; Ming, F.; Liang, H.; Qi, Z.; Liu, W.; Xia, C.; Chen, C.; Cavallo, L.; Wang, Z.; Alshareef, H. N. Preferred Orientation of TiN Coatings Enables Stable Zinc Anodes. *ACS Energy Lett.* **2022**, *7* (1), 197−203.
(41) Han, L.; Guo, Y.; Ning, F.; Liu, X.; Yi, J.; Luo, Q.; Qu, B.; Yue, J.; Lu, Y.; Li, Q. Lotus Effect Inspired Hydrophobic Strategy for Stable Zn Metal Anodes. *Adv. Mater.* **2024**, *36* (11), 2308086.
(42) Zhang, W.; Dong, Q.; Wang, J.; Han, X.; Hu, W. Failure Mechanism, Electrolyte Design, and Electrolyte/Electrode Interface Regulation for Low-Temperature Zinc-Based Batteries. *Small Methods* **2023**, *7* (10), 2300324.
(43) Wang, J.; Hu, H.; Zhang, J.; Li, L.; Jia, L.; Guan, Q.; Hu, H.; Liu, H.; Jia, Y.; Zhuang, Q.; Cheng, S.; Huang, M.; Lin, H. Hydrophobic Lithium Diffusion-Accelerating Layers Enables Long-Life Moisture-Resistant Metallic Lithium Anodes in Practical Harsh Environments. *Energy Storage Mater.* **2022**, *52*, 210−219.
(44) Fu, M.; Zhao, Q.; Long, K.; Li, Q.; Kuang, G. c.; Zhou, L.; Wei, W.; Ji, X.; Chen, L.; Chen, Y. Global "Interface-Space" Dual-Modulation by Functional Supramolecules Organic Frameworks on Aqueous Zinc-Ion Batteries. *Adv. Funct. Mater.* **2024**, *34* (10), 2311680.
(45) Sun, H.; Huyan, Y.; Li, N.; Lei, D.; Liu, H.; Hua, W.; Wei, C.; Kang, F.; Wang, J.-G. A Seamless Metal-Organic Framework Interphase with Boosted $Zn^{2+}$ Flux and Deposition Kinetics for Long-Living Rechargeable Zn Batteries. *Nano Lett.* **2023**, *23* (5), 1726−1734.
(46) Wang, J.; Liu, H.; Zhang, J.; Xiao, Q.; Wang, C.; Zhang, Y.; Liu, M.; Kang, Q.; Jia, L.; Wang, D.; Li, Q.; Duan, W.; Adenusi, H.; Passerini, S.; Zhang, Y.; Lin, H. Polysulfide-Mediated Solvation Shell Reorganization for Fast $Li^+$ Transfer Probed by In-Situ Sum Frequency Generation Spectroscopy. *Energy Storage Mater.* **2024**, *67*, 103289.

(47) Wang, J.; Zhang, J.; Duan, S.; Jia, L.; Xiao, Q.; Liu, H.; Hu, H.; Cheng, S.; Zhang, Z.; Li, L.; Duan, W.; Zhang, Y.; Lin, H. Lithium Atom Surface Diffusion and Delocalized Deposition Propelled by Atomic Metal Catalyst toward Ultrahigh-Capacity Dendrite-Free Lithium Anode. *Nano Lett.* **2022**, *22* (19), 8008−8017.
(48) Wang, J.; Zhang, J.; Wu, J.; Huang, M.; Jia, L.; Li, L.; Zhang, Y.; Hu, H.; Liu, F.; Guan, Q.; Liu, M.; Adenusi, H.; Lin, H.; Passerini, S. Interfacial ″Single-Atom-in-Defects″ Catalysts Accelerating $Li^+$ Desolvation Kinetics for Long-lifespan Lithium Metal Batteries. *Adv. Mater.* **2023**, *35* (39), No. e2302828.
(49) Zhang, J.; He, R.; Zhuang, Q.; Ma, X.; You, C.; Hao, Q.; Li, L.; Cheng, S.; Lei, L.; Deng, B.; Li, X.; Lin, H.; Wang, J. Tuning 4f-Center Electron Structure by Schottky Defects for Catalyzing Li Diffusion to Achieve Long-Term Dendrite-Free Lithium Metal Battery. *Adv. Sci. (Weinh)* **2022**, *9* (23), No. e2202244.
(50) Wang, J.; Li, L.; Hu, H.; Hu, H.; Guan, Q.; Huang, M.; Jia, L.; Adenusi, H.; Tian, K. V.; Zhang, J.; Passerini, S.; Lin, H. Toward Dendrite-Free Metallic Lithium Anodes: From Structural Design to Optimal Electrochemical Diffusion Kinetics. *ACS Nano* **2022**, *16* (11), 17729−17760.
(51) Zhang, J.; You, C.; Lin, H.; Wang, J. Electrochemical Kinetics Modulators in Lithium Sulfur Batteries: from Defect-Rich Catalysts to Single Atomic Catalysts. *Energy Environ. Mater.* **2022**, *5* (3), 731.
(52) Wang, J.; Hu, H.; Duan, S.; Xiao, Q.; Zhang, J.; Liu, H.; Kang, Q.; Jia, L.; Yang, J.; Xu, W.; Fei, H.; Cheng, S.; Li, L.; Liu, M.; Lin, H.; Zhang, Y. Construction of Moisture-Stable Lithium Diffusion-Controlling Layer toward High Performance Dendrite-Free Lithium Anode. *Adv. Funct. Mater.* **2022**, *32* (12), 2110468.
(53) Zhang, X.; Li, X.; Zhang, Y.; Li, X.; Guan, Q.; Wang, J.; Zhuang, Z.; Zhuang, Q.; Cheng, X.; Liu, H.; Zhang, J.; Shen, C.; Lin, H.; Wang, Y.; Zhan, L.; Ling, L. Accelerated $Li^+$ Desolvation for Diffusion Booster Enabling Low-Temperature Sulfur Redox Kinetics via Electrocatalytic Carbon-Grazfted-CoP Porous Nanosheets. *Adv. Funct. Mater.* **2023**, *33* (36), 2302624.
(54) Wang, J.; Zhang, J.; Cheng, S.; Yang, J.; Xi, Y.; Hou, X.; Xiao, Q.; Lin, H. Long-Life Dendrite-Free Lithium Metal Electrode Achieved by Constructing a Single Metal Atom Anchored in a Diffusion Modulator Layer. *Nano Lett.* **2021**, *21* (7), 3245−3253.
(55) He, D.; Cui, W.; Liao, X.; Xie, X.; Mao, M.; Sang, X.; Zhai, P.; Zhao, Y.; Huang, Y.; Zhao, W. Electronic Localization Derived Excellent Stability of Li Metal Anode with Ultrathin Alloy. *Adv. Sci. (Weinh)* **2022**, *9* (10), No. e2105656.
(56) Zhang, K.; Li, C.; Liu, J.; Zhang, S.; Wang, M.; Wang, L. Defect-Rich Functional $HfO_{2-x}$ for Highly Reversible Zn Metal Anode. *Small* **2024**, *20* (14), 2306406.
(57) Jia, L.; Hu, H.; Cheng, X.; Dong, H.; Li, H.; Zhang, Y.; Zhang, H.; Zhao, X.; Li, C.; Zhang, J.; Lin, H.; Wang, J. Toward Low-Temperature Zinc-Ion Batteries: Strategy, Progress, and Prospect in Vanadium-Based Cathodes. *Adv. Energy Mater.* **2024**, *14* (8), 2304010.
(58) Wang, J.; Hu, H.; Jia, L.; Zhang, J.; Zhuang, Q.; Li, L.; Zhang, Y.; Wang, D.; Guan, Q.; Hu, H.; Liu, M.; Zhan, L.; Adenusi, H.; Passerini, S.; Lin, H. Fast Interfacial Electrocatalytic Desolvation Enabling Low-Temperature and Long-Cycle-Life Aqueous Zn Batteries. *InfoMat* **2024**, *6* (7), No. e12558.
(59) Wang, J.; Jia, L.; Duan, S.; Liu, H.; Xiao, Q.; Li, T.; Fan, H.; Feng, K.; Yang, J.; Wang, Q.; Liu, M.; Zhong, J.; Duan, W.; Lin, H.; Zhang, Y. Single Atomic Cobalt Catalyst Significantly Accelerates Lithium Ion Diffusion in High Mass Loading $Li_2S$ Cathode. *Energy Storage Mater.* **2020**, *28*, 375−382.
(60) Zhao, R.; Dong, X.; Liang, P.; Li, H.; Zhang, T.; Zhou, W.; Wang, B.; Yang, Z.; Wang, X.; Wang, L.; Sun, Z.; Bu, F.; Zhao, Z.; Li, W.; Zhao, D.; Chao, D. Prioritizing Hetero-Metallic Interfaces via Thermodynamics Inertia and Kinetics Zincophilia Metrics for Tough Zn-Based Aqueous Batteries. *Adv. Mater.* **2023**, *35* (17), 2209288.
(61) Kao, C.-C.; Ye, C.; Hao, J.; Shan, J.; Li, H.; Qiao, S.-Z. Suppressing Hydrogen Evolution via Anticatalytic Interfaces toward Highly Efficient Aqueous Zn-Ion Batteries. *ACS Nano* **2023**, *17* (4), 3948−3957.
(62) Yang, X.; Fan, H.; Hu, F.; Chen, S.; Yan, K.; Ma, L. Aqueous Zinc Batteries with Ultra-Fast Redox Kinetics and High Iodine Utilization Enabled by Iron Single Atom Catalysts. *Nano-Micro Lett.* **2023**, *15* (1), 126.
(63) Zhang, N.; Huang, S.; Yuan, Z.; Zhu, J.; Zhao, Z.; Niu, Z. Direct Self-Assembly of MXene on Zn Anodes for Dendrite-Free Aqueous Zinc-Ion Batteries. *Angew. Chem., Int. Ed.* **2021**, *60* (6), 2861−2865.
(64) Bao, W.; Liu, L.; Wang, C.; Choi, S.; Wang, D.; Wang, G. Facile Synthesis of Crumpled Nitrogen-Doped MXene Nanosheets as a New Sulfur Host for Lithium-Sulfur Batteries. *Adv. Energy Mater.* **2018**, *8* (13), 1702485.
(65) Li, C.; Cheng, X.; Zhang, Y.; Zhu, J.; Zhou, H.; Yang, Y.; Xu, J.; Wang, J.; Wang, Y.; Yu, H.; Shen, C.; Zhan, L.; Ling, L. Towards Low-Temperature Dendrite-Free Zinc Anode by Constructing Functional MXene Buffer Layer with Duplex Zincophilic Sites. *J. Colloid Interface Sci.* **2024**, *671*, 505−515.
(66) (66) Zhang, M.; Xu, W.; Han, X.; Fan, H.; Chen, T.; Yang, Y.; Gao, Y.; Zheng, C.; Yang, Y.; Xiong, T.; Zhang, Y. W.; Lee, W. S. V.; Wang, W.; Pan, H.; Yu, Z. G.; Xue, J. Unveiling The Mechanism of The Dendrite Nucleation and Growth in Aqueous Zinc Ion Batteries. *Adv. Energy Mater.* **2024**, *14* (9), 2303737.
(67) Zhao, B.; Sun, M.; Chen, F.; Shi, Y.; Yu, Y.; Li, X.; Zhang, B. Unveiling the Activity Origin of Iron Nitride as Catalytic Material for Efficient Hydrogenation of $CO_2$ to $C_{2+}$ Hydrocarbons. *Angew. Chem., Int. Ed.* **2021**, *60* (9), 4496−4500.
(68) Li, G.; Yu, J.; Yu, W.; Yang, L.; Zhang, X.; Liu, X.; Liu, H.; Zhou, W. Phosphorus-Doped Iron Nitride Nanoparticles Encapsulated by Nitrogen-Doped Carbon Nanosheets on Iron Foam In Situ Derived from Saccharomycetes Cerevisiae for Electrocatalytic Overall Water Splitting. *Small* **2020**, *16* (32), 2001980.
(69) Zheng, J.; Zhao, Q.; Tang, T.; Yin, J.; Quilty, C. D.; Renderos, G. D.; Liu, X.; Deng, Y.; Wang, L.; Bock, D. C.; Jaye, C.; Zhang, D.; Takeuchi, E. S.; Takeuchi, K. J.; Marschilok, A. C.; Archer, L. A. Reversible epitaxial electrodeposition of metals in battery anodes. *Science* **2019**, *366* (6465), 645−648.